

Principal curvatures and area ratio of propagating surfaces in isotropic turbulence

Tianhang Zheng and Jiaping You

*State Key Laboratory for Turbulence and Complex Systems, College of Engineering,
Peking University, Beijing 100871, China*

Yue Yang*

*State Key Laboratory for Turbulence and Complex Systems, College of Engineering,
Peking University, Beijing 100871, China
and BIC-ESAT and CAPT, College of Engineering, Peking University, Beijing 100871, China*

(Received 18 April 2017; published 24 October 2017)

We study the statistics of principal curvatures and the surface area ratio of propagating surfaces with a constant or nonconstant propagating velocity in isotropic turbulence using direct numerical simulation. Propagating surface elements initially constitute a plane to model a planar premixed flame front. When the statistics of evolving propagating surfaces reach the stationary stage, the statistical profiles of principal curvatures scaled by the Kolmogorov length scale versus the constant displacement speed scaled by the Kolmogorov velocity scale collapse at different Reynolds numbers. The magnitude of averaged principal curvatures and the number of surviving surface elements without cusp formation decrease with increasing displacement speed. In addition, the effect of surface stretch on the nonconstant displacement speed inhibits the cusp formation on surface elements at negative Markstein numbers. In order to characterize the wrinkling process of the global propagating surface, we develop a model to demonstrate that the increase of the surface area ratio is primarily due to positive Lagrangian time integrations of the area-weighted averaged tangential strain-rate term and propagation-curvature term. The difference between the negative averaged mean curvature and the positive area-weighted averaged mean curvature characterizes the cellular geometry of the global propagating surface.

DOI: [10.1103/PhysRevFluids.2.103201](https://doi.org/10.1103/PhysRevFluids.2.103201)

I. INTRODUCTION

A propagating surface in fluid flow evolves with a local fluid velocity and a displacement velocity normal to itself. It has been used to model the flame front [1–3] that can be defined as an isosurface of the temperature or product concentration in turbulent premixed combustion. In this context, the surface propagates from burnt products towards fresh reactants. The model based on propagating surfaces assumes that the thickness and the thermochemistry time scale of a premixed flame front in the flamelet regime are much smaller than Kolmogorov scales of turbulence. Hence, the influence of molecular diffusion and chemical reaction on the motion of the flame front is only via the displacement velocity, which is usually modeled as a constant or a function of the local strain rate and curvature on the surface for weakly stretched flames [4,5].

The evolution of a global propagating surface can be formulated mathematically by two approaches. In the Eulerian level-set approach, the surface is extracted as an isosurface of a scalar function, and the scalar is evolved through a partial differential equation [3,4,6,7]. In the local Lagrangian one-point description, the surface consists of a number of propagating surface elements

*yyg@pku.edu.cn

(or flamelets in the combustion context), and each surface element evolves independently via a set of ordinary differential equations for Lagrangian quantities [1,2]. The present study adopts the latter Lagrangian approach, because it appears to be more natural than the Eulerian approach to describe flame wrinkling with a “memory” of any wrinkling occurring upstream [8] and highly localized phenomena such as local extinction and pocket formation [9].

The curvatures and surface area ratio of a propagating surface are of practical value in the study of premixed combustion. In general, turbulence tends to wrinkle the flame front, which increases the flame area and the probability of cusp formation and quenching [10,11]. The local curvatures of flame fronts characterize the wrinkling of a flame front [12], and they are closely related to the local displacement velocity [13,14]. Both direct numerical simulation (DNS) results and experimental data show that the probability density function (PDF) of the mean curvature of a flame front is close to a Gaussian distribution with a zero mean and a slight skewness to the negative side [15–17]. The joint PDFs of principal curvatures of flame fronts are used to investigate the influence of the curvatures on the heat release rate and displacement velocity [18,19].

The surface area ratio, another metric of flame wrinkling, is the ratio of the flame surface area in turbulence divided by its projection in the propagating direction [5]. This ratio generally determines the increase of the turbulent burning velocity compared with the laminar flame velocity, because the increase of the total flame surface allows a higher consumption rate for the same cross section. In numerical studies, the area ratio is modeled as the averaged magnitude of the gradient of the temperature or progress variable, and then its evolution equation is derived with some physical assumptions [20,21]. In experimental studies, the area ratio is modeled by empirical fits from the measurement and image processing [22,23]. On average, the flame surface area is increased by the tangential strain rate and is decreased by the local curvature [24,25]. Although there are a variety of empirical models for predicting the flame area ratio and the related turbulent burning velocity, the predictions provided by different models cannot collapse owing to the lack of a rigorous theoretical framework and unique definition, and the uncertainty of different measurement methods and boundary geometries [8,26].

Besides the local geometry, the topology of propagating surfaces is also of interest in premixed combustion. A propagating surface with a constant displacement speed can generate a cusp with infinite curvature in a finite time [1,2], which is essentially different from a material surface that cannot form a cusp [27,28]. Although artificial cusps are smoothed by diffusion and curvature effects in real combustion, their formation process involves the generation of a region with large negative curvatures. This is similar to the pocket formation [9] due to the very large local tangential strain rate on a flame front, and is related to the cellular geometry in premixed flames. The cellular structure manifests the large-scale and small-scale flame fronts tending to be convex and concave to reactants, respectively. The generation of the cellular flame front is of importance in predicting the flame stabilization and pollutant emission [29].

Since the turbulence-chemistry interaction is too complex for theoretical analysis, the propagating surface as a simple Lagrangian-based model is useful to decouple the diffusion and chemical reaction from the hydrodynamics effect on turbulent premixed combustion in the flamelet regime. We remark that the flow in the present study has constant density and viscosity, unlike in flames with large variations of thermodynamic properties. Moreover, we can neither detect the annihilation of adjacent regular parts of the propagating surface nor describe the evolution of cusps generated by the surface self-intersection [1]. In spite of these limitations, this model can elucidate the effect of the Reynolds number and displacement velocity on curvature statistics and area ratio. A deep understanding of the behavior of propagating surfaces can be helpful for the modeling of turbulent premixed combustion in general, e.g., flamelet-like models [4] and flame-surface-density models [24,30], and the turbulent burning velocity in particular. In addition, the computational cost for this model is much lower than that of DNS and large-eddy simulation (LES) of turbulent combustion, which can facilitate the parametric study for turbulent flames [3,30].

Therefore, the study of propagating surfaces in isotropic turbulence is revisited. In the present study, we aim to reveal the non-local geometry (in the surface sense) [31,32] in the evolution of

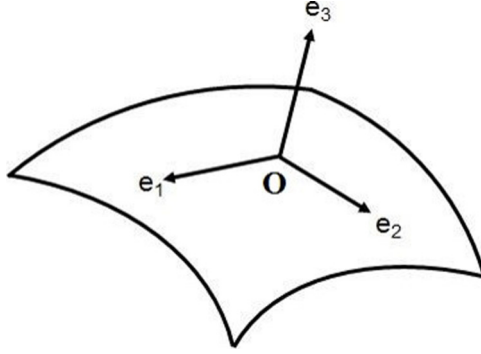


FIG. 1. Local coordinates on a propagating surface element.

the global propagating surface, and to partially bridge the gap between the Lagrangian studies in nonreacting turbulence [31,33] and turbulent premixed combustion [34,35]. Compared with the prior study investigating propagating surface elements that are randomly distributed in isotropic turbulence at a low Reynolds number [2], the present study makes original contributions as follows. (1) A revised numerical method is developed to calculate principal curvatures of propagating surfaces. (2) The effects of a range of Reynolds numbers and displacement speeds on curvature statistics are studied. (3) The global propagating surface consisting of the surface elements initially arranged on a planar surface is used to mimic a premixed flame in turbulence, and its nonlocal geometry is characterized. (4) A model for the surface area ratio of the global surface is developed based on area-weighted averages of tangential strain rate and mean curvature.

The outline of this paper is as follows. In Sec. II, the governing equations for fluid flow and propagating surface elements are provided. In Sec. III, the numerical methods for simulating isotropic turbulence and tracking propagating surfaces are described. In Sec. IV, the effects of the Reynolds number and dimensionless displacement speed on statistics of principal curvatures are investigated. In Sec. V, the evolution equation of the area ratio of a global propagating surface is developed, along with the characterization of the cellular geometry of the surface. Some conclusions are drawn in Sec. VI.

II. GOVERNING EQUATIONS

The properties of interest for a propagating surface element include the location, local coordinates, curvature tensor, and surface area, and their evolution equations are derived by Pope [1]. The governing equation of the location $\mathbf{X}(t)$ of a propagating surface element is

$$\frac{d\mathbf{X}(t)}{dt} = \mathbf{U}(\mathbf{X}(t),t) + S_d(\mathbf{X}(t),t)\mathbf{n}(\mathbf{X}(t),t). \quad (1)$$

Each surface element moves with the local fluid velocity \mathbf{U} and displacement velocity $S_d\mathbf{n}$ independently. Here, $\mathbf{U}(\mathbf{X}(t),t)$ is equal to the Eulerian velocity $\mathbf{u}(\mathbf{x} = \mathbf{X}(t),t)$ that is governed by constant-density, incompressible Navier-Stokes (NS) equations,

$$\frac{\partial u_i}{\partial x_i} = 0, \quad \frac{\partial u_i}{\partial t} + u_j \frac{\partial u_i}{\partial x_j} = -\frac{1}{\rho} \frac{\partial p}{\partial x_i} + \nu \frac{\partial^2 u_i}{\partial x_j^2} + f_i, \quad i, j = 1, 2, 3, \quad (2)$$

where ρ denotes a constant density, ν and p denote the kinematic viscosity and pressure respectively, and f_i is an external forcing term. In the displacement velocity $S_d\mathbf{n}$, S_d denotes the displacement speed and \mathbf{n} the unit normal of the surface element.

To calculate \mathbf{n} and other geometric properties of a surface element, a local Cartesian coordinate system $\mathbf{e}_i(\mathbf{X}(t),t)$, $i = 1, 2, 3$, moving with a surface element is applied; it is sketched in Fig. 1. Its

origin denoted by “O” is at the position $X(t)$ of the surface element. The governing equations for this coordinate system are

$$\frac{d\mathbf{e}_3}{dt} = -\mathbf{e}_\alpha U_{3,\alpha}, \quad \frac{d\mathbf{e}_\alpha}{dt} = \frac{1}{2} \mathbf{e}_\beta (U_{\beta,\alpha} - U_{\alpha,\beta}) + \mathbf{e}_3 U_{3,\alpha}, \quad \alpha, \beta = 1, 2, \quad (3)$$

where \mathbf{e}_3 is the unit normal vector, equivalent to \mathbf{n} in Eq. (1), \mathbf{e}_1 and \mathbf{e}_2 are two orthogonal unit vectors in the tangent plane, and “ α ” denotes the partial derivative with respect to y_α , that is, the coordinate in the direction of \mathbf{e}_α .

The curvature tensor

$$h_{\alpha\beta} \equiv \frac{\partial^2 h}{\partial y_\alpha \partial y_\beta} \quad (4)$$

is a second-order symmetric tensor obtained by differentiating a height function $h(y_1, y_2, t)$ with respect to y_α and y_β , where h is the height of a point located at (y_1, y_2) on a surface element above its tangent plane at O. The governing equation of $h_{\alpha\beta}$ is

$$\frac{dh_{\alpha\beta}}{dt} = s_{33}h_{\alpha\beta} - (s_{\gamma\beta}h_{\alpha\gamma} + s_{\gamma\alpha}h_{\beta\gamma}) + (U_{3,\alpha\beta} + S_{d,\alpha\beta}) + S_d h_{\alpha\gamma} h_{\gamma\beta}, \quad (5)$$

where

$$s_{ij} \equiv \frac{1}{2} \left(\frac{\partial U_i}{\partial y_j} + \frac{\partial U_j}{\partial y_i} \right), \quad i, j = 1, 2, 3 \quad (6)$$

is the local rate-of-strain tensor. From the eigenvalues k_i of $h_{\alpha\beta}$, $i = 1, 2$, we define the principal curvatures as $\kappa_i = -k_i$ of the surface element at O with $\kappa_1 > \kappa_2$. Namely, the surface element convex (or concave) to the propagating direction \mathbf{n} has a positive (or negative) curvature.

The governing equation for k_i can be derived from Eq. (5) as

$$\frac{dk_i}{dt} = m_{i\alpha} m_{i\beta} [U_{3,\alpha\beta} + S_{d,\alpha\beta} + s_{33}h_{\alpha\beta} - (s_{\gamma\beta}h_{\alpha\gamma} + s_{\gamma\alpha}h_{\beta\gamma}) + S_d h_{\alpha\gamma} h_{\gamma\beta}], \quad (7)$$

where the index i is excluded from the summation convention and the second-order tensor m_{ij} denotes the principal axis transformation of $h_{\alpha\beta}$. Assuming a constant S_d and normalizing velocity derivatives by Kolmogorov length scale η and time scale τ_η , the scale analysis of the magnitude of principal curvatures in Eq. (7) yields

$$\frac{d\kappa_i^*}{dt^*} = b_1 + b_2 \kappa_i^* + b_3 S_d^* \kappa_i^{*2}, \quad (8)$$

where $\kappa_i^* \equiv \kappa_i \eta$, $t^* \equiv t/\tau_\eta$, and $S_d^* \equiv S_d/u_\eta$ are dimensionless quantities. The three terms in the right-hand side (RHS) of Eq. (8) represent the rate of bending of the surface, the action of strain to modify existing curvature, and the rate of change of curvature due to the propagation of the surface [1], and their coefficients b_1 , b_2 , and b_3 are expected to be stationary random variables with the order $O(1)$ in stationary isotropic turbulence.

The evolution equation for the surface area δA or the stretch rate $K \equiv \ln \delta A$ of each surface element is

$$\frac{d \ln \delta A}{dt} = K_t + 2S_d \kappa, \quad (9)$$

where

$$K_t \equiv U_{1,1} + U_{2,2} \quad (10)$$

is the tangential strain rate and $\kappa \equiv \frac{1}{2}(\kappa_1 + \kappa_2)$ is the mean curvature. Equation (9) can be re-expressed by nondimensionalizing the variables by Kolmogorov scales as

$$\frac{d \ln \delta A}{dt^*} = K_t^* + 2S_d^* \kappa^*, \quad (11)$$

TABLE I. Summary of DNS parameters.

Number of grids	N^3	256^3	256^3	512^3
Kinematic viscosity	ν	7×10^{-3}	3.5×10^{-3}	1.2×10^{-3}
Total kinetic energy	$E_{\text{tot}} = \sum_k \langle \hat{\mathbf{u}} \cdot \hat{\mathbf{u}}^* \rangle / 2$	0.97	1.10	1.12
Mean dissipation rate	$\epsilon = 2\nu \sum_k \langle k^2 \hat{\mathbf{u}} \cdot \hat{\mathbf{u}}^* \rangle$	0.15	0.19	0.20
Root-mean-square fluctuation	$u' = (2E_{\text{tot}}/3)^{1/2}$	0.80	0.86	0.86
Taylor length scale	$\lambda = (15\nu u'^2/\epsilon)^{1/2}$	0.66	0.44	0.26
Taylor Reynolds number	$\text{Re}_\lambda = u'\lambda/\nu$	76	110	185
Turbulent Reynolds number	$\text{Re} = u' L_e/\nu$	192	373	1109
Integral length scale	$L_e = (\pi/2u'^2) \int dk E(k)/k$	1.68	1.52	1.48
Eddy turnover time	$T_e = L_e/u'$	2.08	1.76	1.71
Kolmogorov length scale	$\eta = (\nu^3/\epsilon)^{1/4}$	0.0386	0.0215	0.0096
Kolmogorov time scale	$\tau_\eta = (\nu/\epsilon)^{1/2}$	0.21	0.13	0.077
Kolmogorov velocity scale	$u_\eta = \eta/\tau_\eta$	0.184	0.165	0.125
Spatial resolution	$k_{\text{max}}\eta$	3.3	1.8	1.6

where $\kappa^* \equiv \kappa\eta$ and $K_t^* \equiv K_t\tau_\eta$ are dimensionless mean curvature and tangential strain rate, respectively.

III. NUMERICAL METHODS

A. DNS

In the DNS of stationary homogeneous isotropic turbulence in a periodic box of side $L = 2\pi$, the NS equation (2) is solved by a standard pseudospectral method [31,36] at three Taylor micro-scale Reynolds numbers, $\text{Re}_\lambda = 76, 110, \text{ and } 185$. The flow is driven by the random forcing term $f_i(\mathbf{x}, t)$ on the Fourier modes with the wave number magnitude $k \equiv |\mathbf{k}|$ less than 2, and the energy spectrum $E(k)$ with $k < 2$ is forced to satisfy the $-5/3$ law. The flow domain is discretized uniformly on N^3 grids. Aliasing errors are removed using the two-thirds truncation method as the maximum wave number $k_{\text{max}} \approx N/3$. The Fourier coefficient $\hat{\mathbf{u}}(\mathbf{k}, t)$ of the velocity in Fourier space is advanced in time using a second-order Adams-Bashforth method, and the time step is chosen to ensure that the Courant-Friedrichs-Lewy number is less than 0.5.

The DNS parameters are listed in Table I. The total turbulent kinetic energy is controlled around $E_{\text{tot}} \approx 1$ by the external forcing f_i in Eq. (2). The spatial resolution $k_{\text{max}}\eta$ in the spectral simulation is greater than 1.5 to ensure numerical accuracy. We remark that a higher resolution is generally required as the Reynolds number increases [37,38]. Normalized energy spectra at three Re_λ are shown in Fig. 2. The spectrum for $\text{Re}_\lambda = 76$ decays rapidly from the artificially imposed $k^{-5/3}$ spectrum, and the spectra for $\text{Re}_\lambda = 110$ and 185 have short inertial ranges at $k\eta \sim O(10^{-1})$.

B. Tracking of propagating surface elements

The tracking of propagating surface elements begins at $t = 0$ when the turbulent flow has reached the statistically stationary state. The tracking algorithm is adapted from the method of Girimaji and Pope [2]. The second-order Runge-Kutta scheme is applied to advance Eqs. (1), (3), and (9) explicitly and Eq. (5) implicitly in time for the evolution of the location, local coordinates, surface area, and curvature tensor of a surface element, respectively. The time increment is selected to capture the finest resolved scales in the velocity field. The first and second derivatives of the velocity required in these equations are calculated by the spectral method, where the numerical errors involved have been verified to be negligibly small with the current resolution $k_{\text{max}}\eta > 1.5$ [27]. A three-dimensional sixth-order Lagrangian interpolation scheme [36] is used to calculate the Lagrangian velocity $\mathbf{U}(\mathbf{X}(t), t)$ at the location of a surface element from the Eulerian velocity

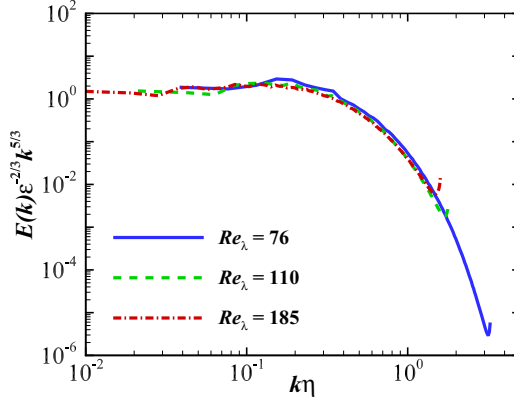


FIG. 2. Normalized energy spectra.

calculated from DNS. The former numerical tests [39] demonstrate that the numerical error of the interpolation from Eulerian values to Lagrangian ones is less than 1% with the current resolution. Additionally, if a surface element at $X(t)$ moves out of the computational domain, the Lagrangian velocity and its first and second derivatives of the element are evaluated at the reference location $X'(t)$ in the domain of box turbulence using periodic boundary conditions. Here, the coordinates of the reference location are $X'_i = X_i - 2\pi \lfloor X_i/(2\pi) \rfloor$, $i = 1, 2, 3$, where $\lfloor \cdot \rfloor$ denotes the floor function.

In the numerical implementation, we find that the curvature tensor $h_{\alpha\beta}$ can be slightly asymmetric using the existing numerical method [2] owing to the accumulation of numerical errors. This results in imaginary principal curvatures calculated from $h_{\alpha\beta}$, so the time marching method for Eq. (5) is revised to impose the symmetry of the curvature tensor. Moreover, the propagating surface elements can evolve into cusps after a finite time [2], and the cusps can be smoothed out or can induce local extinction in real combustion. The numerical implementation of the revised Runge-Kutta method and the criterion for detecting cusps are described in the Appendix in detail.

We remark that the term $S_{d,\alpha\beta}$ in Eq. (5) is ignored in the present simulation for the evolution of initially planar surface elements at short times, which is further justified in Sec. IV D. Although S_d can depend on the curvature tensor in premixed combustion, this is challenging for the numerical calculation of $S_{d,\alpha\beta}$ with fourth-order derivatives of velocity under satisfactory resolution.

C. Reconstruction of the global propagating surface

At the initial time, N_e surface elements are uniformly arranged on an x - y plane at $z = \pi$ to model a propagating planar flame in premixed combustion. At the initial tracking time $t = 0$, each surface element has $(\mathbf{e}_1, \mathbf{e}_2, \mathbf{e}_3) = (0, 0, 1)$, $h_{\alpha\beta} = 0$, and the initial surface area ratio $\delta A/\delta A_0 = 1$.

In the present study, we set $N_e = 128^2$, and tag each element as (m_e, n_e) with $1 \leq m_e, n_e \leq \sqrt{N_e}$. The neighboring elements of (m_e, n_e) are tagged by $(m_e \pm 1, n_e)$ and $(m_e, n_e \pm 1)$ at the initial time. In order to track the evolution of the global propagating surface consisting of surface elements, the order of the element tags is recorded at each time step. The locations of all the elements are stored one by one from the element tag $(1, 1)$ to $(\sqrt{N_e}, \sqrt{N_e})$ in a file, then the file is loaded by the visualization software TECPLOT [40] to visualize the global surface by connecting the surface elements based on the tag order at a given time.

We remark that this method is only feasible at the early stage of the evolution of a global propagating surface, when the global surface has no significant topological change. Moreover, this reconstruction is only useful for visualization, and has no influence on the statistical study of propagating surface elements.

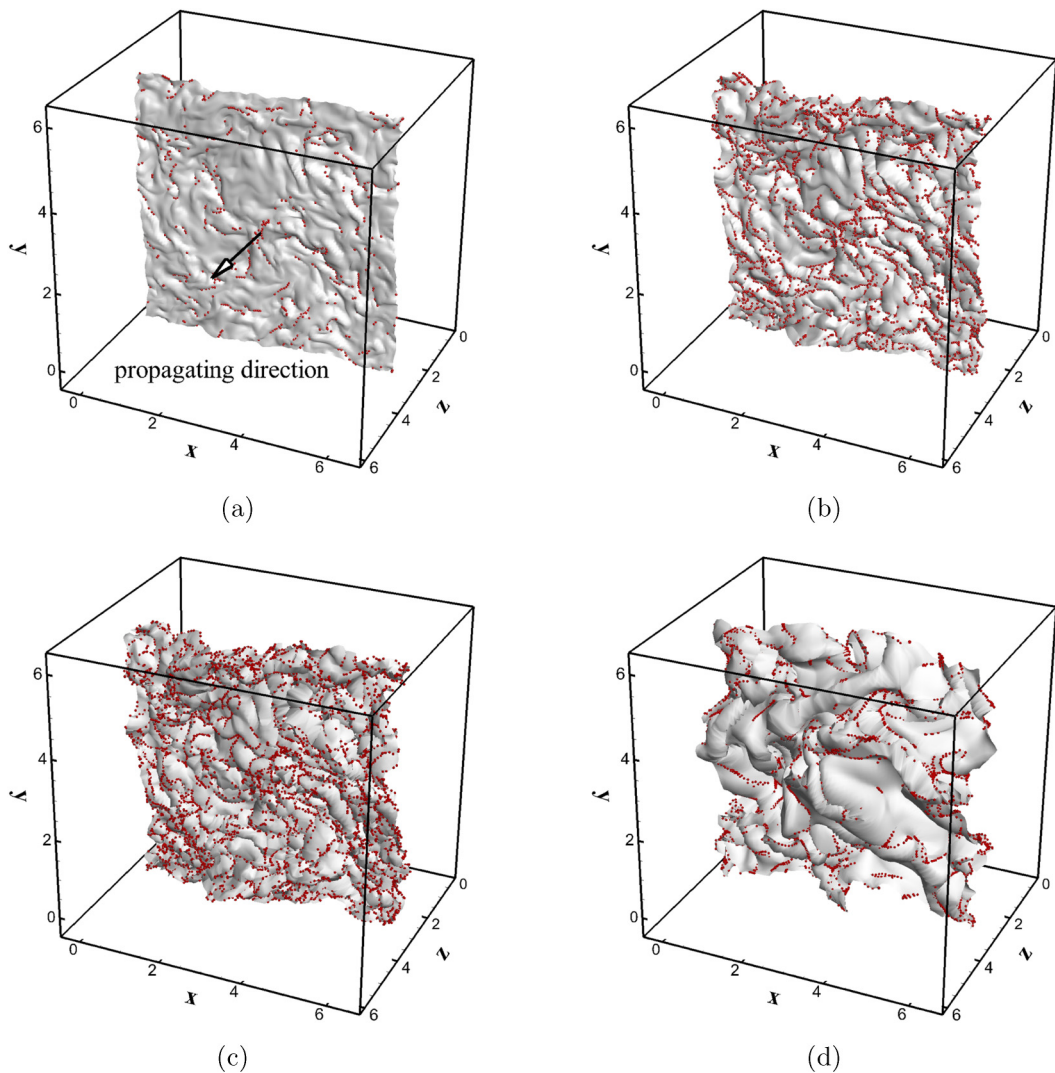


FIG. 3. Global propagating surfaces initially consisting of 128^2 surface elements with $S_d/u' = 1.0$ at different times and Taylor Reynolds numbers in isotropic turbulence. The red dots mark the locations of cusp generation. (a) $t/\tau_\eta = 1$, $Re_\lambda = 185$, (b) $t/\tau_\eta = 2$, $Re_\lambda = 185$, (c) $t/\tau_\eta = 3$, $Re_\lambda = 185$, and (d) $t/\tau_\eta = 3$, $Re_\lambda = 110$.

IV. PRINCIPAL CURVATURES

A. Evolution of curvature statistics

The evolution of a global propagating surface consisting of surface elements in stationary homogeneous isotropic turbulence with constant $S_d/u' = 1.0$ is shown in Figs. 3(a)–3(c). From an initial plane, the propagating surface is gradually wrinkled and corrugated by turbulent straining motion to form the cellular geometry. Compared with the persistent stretch of a passive material surface [31], the evolution of a propagating surface with a constant S_d can generate cusps in finite time [1,2], and the locations of the cusp are marked by red dots. As shown in Fig. 4, we zoom in on Fig. 3(b) and observe from the back of the surface towards the propagating direction. Most of the cusps are generated around the “crest” of the surface where there are large negative curvatures.

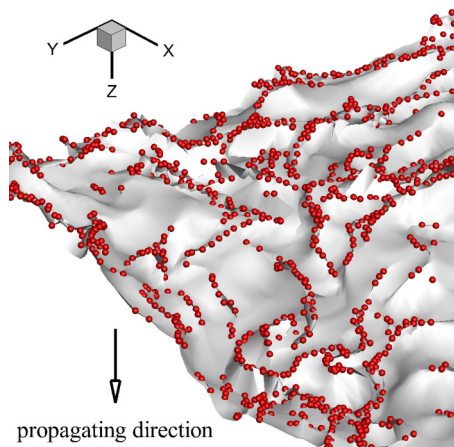


FIG. 4. Formation of cusps marked by red dots on the global propagating surface with large negative curvatures (concave to the propagating direction), which is a zoom-in view of Fig. 3(b) from a different perspective.

This is also referred to as the pocket structure, which is critical for predicting the flame stabilization and pollutant formation in turbulent premixed combustion [9]. A schematic diagram for the cusp formation in the evolution of propagating surfaces is illustrated in Fig. 5.

If the curvature effect on the surface with a Markstein length [4,5] is considered in the modeling of the displacement speed, the cusps can be smoothed, but some parts of the surface can still have large curvatures resulting in local extinctions in premixed flames. Furthermore, recent studies using flame particle tracking show that the flame particles, defined as points on the flame front, can partly disappear owing to the cusp formation [19,34]. The numbers of the disappeared elements that have already evolved into cusps and the “surviving” elements are denoted by N_d and $N_s \equiv N_e - N_d$, respectively. We find that the principal curvatures of most of the N_s surviving elements are restricted to

$$-1/\eta \leq \kappa_1, \quad \kappa_2 \leq 1/\eta, \quad (12)$$

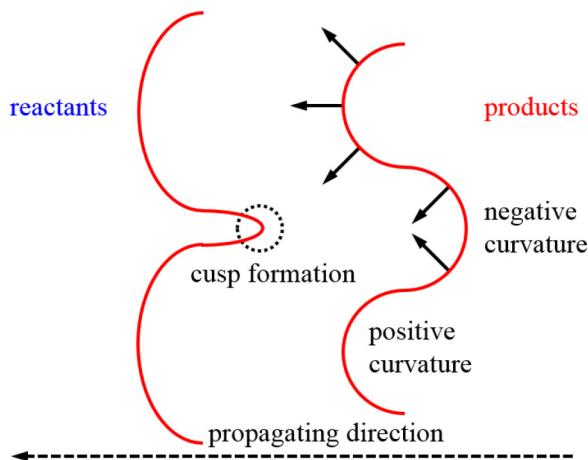


FIG. 5. The schematic diagram for the cusp formation in the evolution of propagating surfaces represented by red lines. The dotted circle identifies the location of the cusp, and the solid arrows show the local propagating direction. The dashed arrow denotes the propagating direction of the global surface.

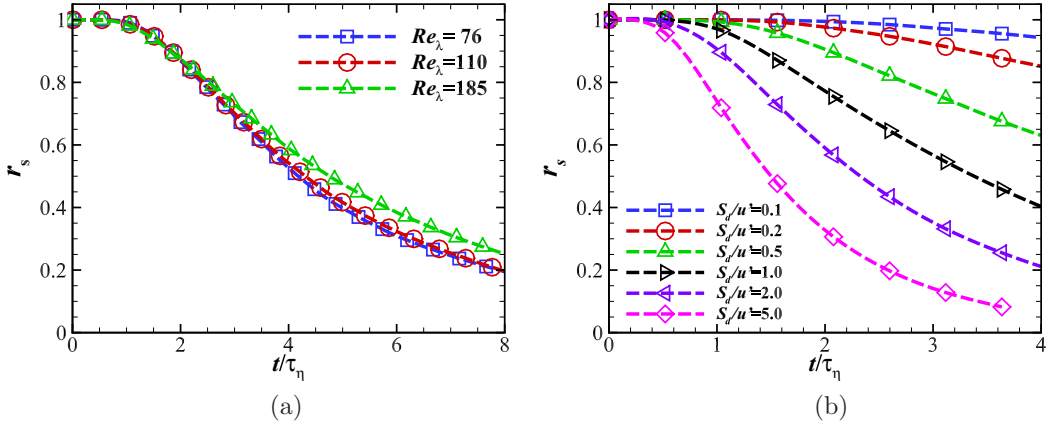


FIG. 6. Evolution of the ratio of surviving surface elements in isotropic turbulence with different displacement speeds and Taylor Reynolds numbers. (a) $S_d/u_\eta = 4.0$ and (b) $Re_\lambda = 185$.

so the elements with curvatures out of this range tend to evolve into cusps in the next few time steps, and those extreme sample values cannot exist owing to the smoothing effect of diffusion and curvature in real frames. Therefore, in the present statistical study of principal curvatures, we only consider the surviving surface elements satisfying Eq. (12) to prevent the extreme sample values from making a disproportional contribution to the curvature statistics.

The surviving ratio $r_s \equiv N_s/N_e$ of surface elements is shown in Fig. 6. The cusp generation occurs around $t/\tau_\eta = 1.0$. The cusps are generated more quickly at larger displacement speeds, which is discussed in following subsections. In Fig. 7, the mean and variance of principal curvatures reach a statistically stationary state at $t = T_s \approx 2\tau_\eta$, which are key features to characterize the deformation of the global propagating surface.

B. Self-similarity

The mean and variance of principal curvatures in isotropic turbulence with three Reynolds numbers and a range of constant displacement speeds from $S_d/u' = 0.1$ to 5.0 are shown in Figs. 8(a)

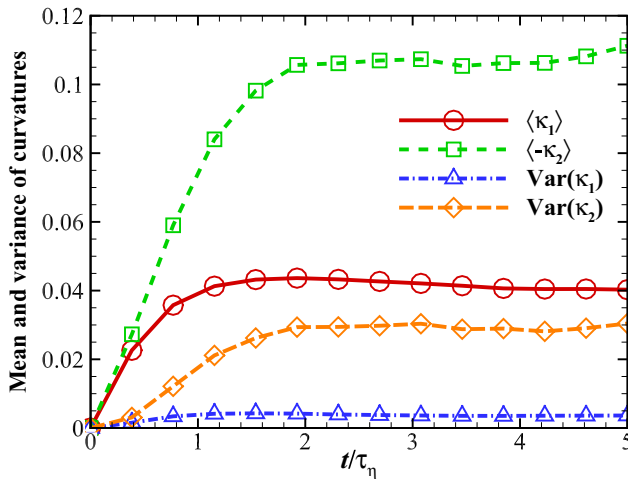


FIG. 7. Evolution of curvature statistics in isotropic turbulence with $Re_\lambda = 110$ and $S_d/u' = 1.0$.

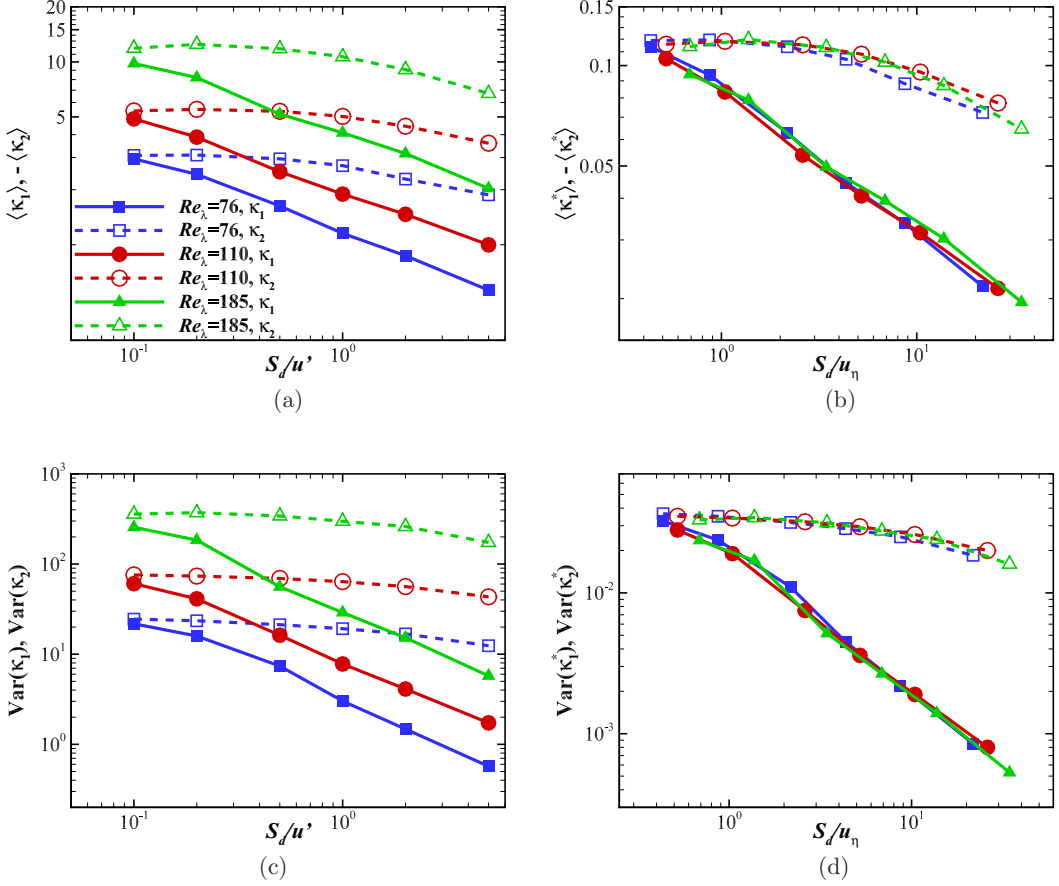


FIG. 8. Statistics of the principal curvatures in isotropic turbulence with different Taylor Reynolds numbers and displacement speeds. (a) mean, (b) normalized mean, (c) variance, and (d) normalized variance.

and 8(c), where S_d scaled by u' is commonly used in the study of premixed combustion. The statistics are estimated over an ensemble of N_s surviving surface elements in the statistical stationary state. In general, we find $\langle \kappa_1 \rangle > 0$ and $\langle \kappa_2 \rangle < 0$ with $|\langle \kappa_1 \rangle| < |\langle \kappa_2 \rangle|$, because propagation tends to increase the radius of curvature for a surface with a positive curvature (see Fig. 5), whereas it tends to flatten out a surface with a negative curvature [1]. The averaged principal curvatures imply that the averaged mean curvature is slightly negative. For the same displacement speed, the means and variances of principal curvatures for high Reynolds numbers are larger than the ones for low Reynolds numbers. This agrees with the visualization in Figs. 3(c) and 3(d). The global propagating surface at $Re_\lambda = 185$ is more wrinkled than that at $Re_\lambda = 110$.

On the other hand, we find that if the principal curvatures and displacement speed are normalized by Kolmogorov scales, the statistical profiles for different Reynolds numbers in Figs. 8(a) and 8(c) collapse in Figs. 8(b) and 8(d). This indicates that the curvature distribution of the wrinkling propagating surfaces is self-similar for different Reynolds numbers. The self-similarity of curvature statistics is supported by the theoretical analysis of Eq. (8), in which the normalized principal curvatures κ_1^* and κ_2^* only depend on S_d^* rather than the Reynolds number in Fig. 8. Similarly, the surviving ratio for a normalized displacement speed S_d^* is also almost independent of the Reynolds number in Fig. 6(a).

The joint PDF of the principal curvatures of surface elements in the statistically stationary state is shown in Fig. 9. The two principal curvatures have a weak positive correlation, and the global

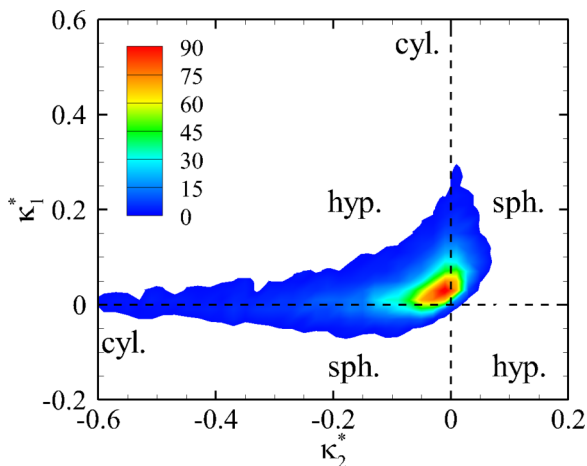


FIG. 9. Joint PDF of principal curvatures of propagating surface elements in isotropic turbulence with $Re_\lambda = 110$ and $S_d/u' = 1.0$. The geometry of the propagating surface element is spherical for $\kappa_1/\kappa_2 = 1$, hyperboloidal for $\kappa_1/\kappa_2 = -1$, and cylindrical for $\kappa_1/\kappa_2 = 0$ or $\kappa_2/\kappa_1 = 0$.

propagating surface is mostly composed of hyperboloidal and cylindrical geometries. In particular, the highly curved elements with a very large principal curvature tend to be cylindrical, which agrees with the asymptotic behavior of curvature for material surfaces [27,41] and propagating surfaces [2] at long times. The PDF shape of principal curvatures in Fig. 9 is consistent with those of flame fronts from DNS of premixed combustion [18,19]. Additionally, the PDF of the mean curvature is close to a Gaussian distribution with a small negative skewness (not shown), which also agrees with the result in combustion [15–17]. These similarities demonstrate that the statistical result obtained from propagating surfaces can be useful in the study of premixed turbulent flames.

C. Effect of the constant displacement speed

The behavior of the solution of Eq. (8) has been extensively discussed [1,2]. If the last term in Eq. (8) dominates, the surface element with a large negative curvature κ_i^* can develop a singularity with infinite curvature in a finite time,

$$t_\infty \approx (\kappa_i^* S_d^*)^{-1}. \quad (13)$$

In Fig. 8, the order of the averaged $|\kappa_i^*|$ is $O(0.1)$, so the propagation term appears to dominate if the order of S_d^* is larger than $O(10)$. This supports the result that the surviving ratio drops significantly as $S_d^* \geq 6.4$ or $S_d/u' \geq 0.5$ in Fig. 6(b). On the other hand, the relatively small positive principal curvature on a surface element is difficult to evolve into a singularity.

Compared with the effect of the Reynolds number, the effect of the normalized displacement speed appears to be complicated. In Figs. 8(b) and 8(d), both $|\langle \kappa_i^* \rangle|$ and variance of κ_i^* decrease with increasing S_d^* . In particular, $|\langle \kappa_1^* \rangle|$ decreases exponentially with increasing S_d^* because propagation tends to decrease positive curvatures, as shown in Fig. 5, and $|\langle \kappa_2^* \rangle|$ decreases more mildly than $|\langle \kappa_1^* \rangle|$ partly due to the cusp formation. Since the increasing S_d^* in Eq. (13) accelerates the process that the surface element with a large negative principal curvature evolves into a cusp at $t = t_\infty$, less surface elements with large $|\langle \kappa_2^* \rangle|$ can survive, and they are excluded in the statistical study.

D. Effect of the nonconstant displacement speed

In the study of premixed flames, the constant displacement speed should be modified to account for the effect of flame stretch. From the asymptotic theory, the first-order correction term for small

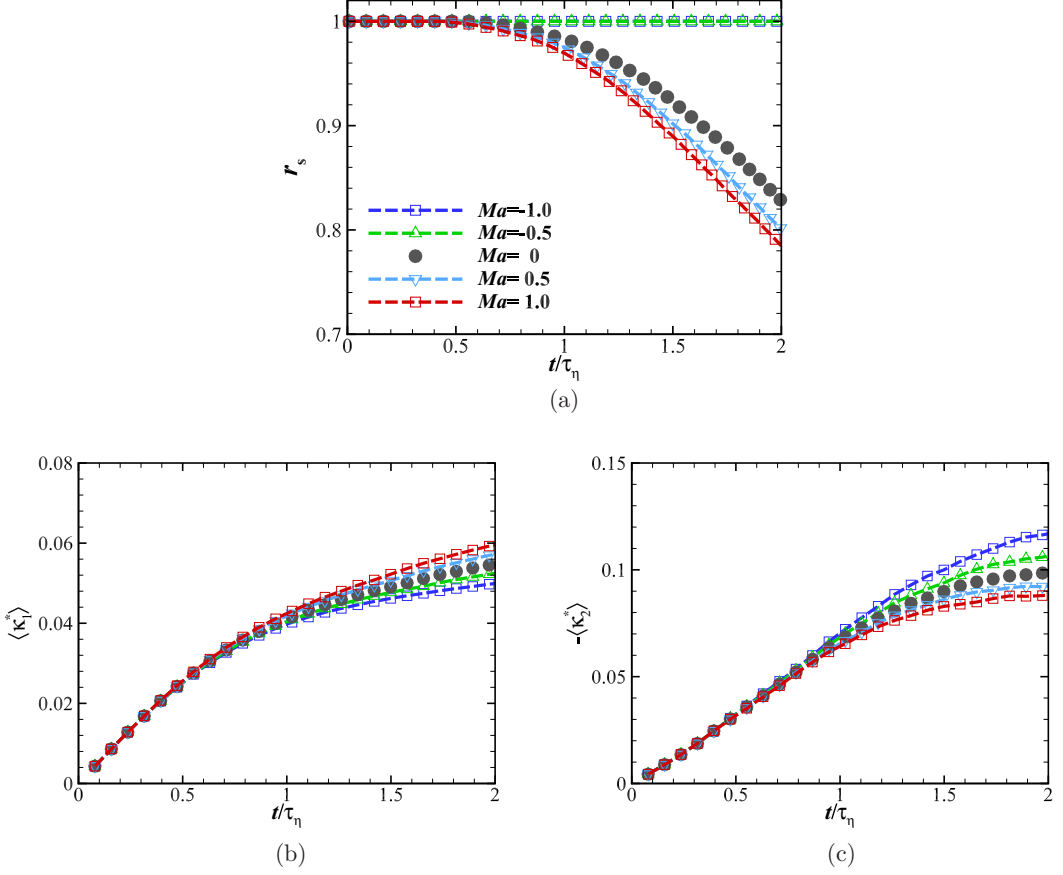


FIG. 10. Temporal evolution of statistics of propagating surface elements with different Markstein numbers in isotropic turbulence with $Re_\lambda = 110$, $S_L/u' = 1.0$, and $Ka = 0.1$. (a) surviving ratio, (b) $\langle \kappa_1^* \rangle$, and (c) $-\langle \kappa_2^* \rangle$.

curvature and strain rate is added in the modified displacement speed [4,5,13] as

$$S_d = S_L - \mathcal{L}K = S_L(1 - Ma Ka K^*). \quad (14)$$

In the combustion context, S_L is a constant unstrained laminar flame speed; $Ma \equiv \mathcal{L}/\delta_L$ is the Markstein number which denotes the ratio of the Markstein length \mathcal{L} to the laminar flame thickness δ_L and measures the sensitivity of the flame speed to the local flame stretch, and Ma can be positive or negative depending on the fuel-air mixture and equivalence ratio; $Ka \equiv t_L/\tau_\eta$ is the Karlovitz number as the ratio of the laminar flame time scale $t_L \equiv \delta_L/S_L$ to the Kolmogorov time scale.

In order to evaluate the variation of S_d in the wrinkling process of the propagating surface, Eq. (14) is dimensionalized and rearranged as

$$S_d^* - S_L^* = -Ma Ka [(K_t^* + S_L^* \kappa_1^*) + S_L^* \kappa_2^*] \quad (15)$$

with $S_L^* \equiv S_L/u_\tau$. In the RHS of Eq. (15), K_t^* and κ_1^* are statistically positive, and κ_2^* is statistically negative [2,19].

The limitation of the displacement speed model Eq. (14) for studying premixed flames is $Ka \ll 1$. We set $Ka = 0.1$ to satisfy this restriction and show the notable effect of $Ma Ka$ on curvature statistics by varying Ma from -1 to 1 . The temporal evolution of statistics for different Ma are shown in Fig. 10. In the asymptotic limit of the laminar flame sheet, for example, a fuel-lean hydrogen-air flame has $Ma \leq 0$ and a methene-air flame has $Ma \approx 1$ [42].

We remark that Eq. (5) without $S_{d,\alpha\beta}$ is still used, and this approximation is only appropriate for very small times and Ma Ka . The scale analysis of the magnitude of principal curvatures in Eq. (7) with the model Eq. (14) of S_d yields

$$\frac{d\kappa_i^*}{dt^*} = c_1 + c_2\kappa_i^* + c_3S_L^*\kappa_i^{*2} - \text{Ma Ka } S_L^*[c_3(\kappa_1^* + \kappa_2^*)\kappa_i^{*2} + 2S_L^*\kappa_{i,\alpha\beta}^*], \quad (16)$$

where the coefficients c_1 , c_2 , and c_3 are expected to be stationary random variables with the order $O(1)$ in stationary isotropic turbulence. The last term in the RHS of Eq. (16) is derived by normalizing $S_{d,\alpha\beta}$ in Eq. (7). At very small times, the bending term c_1 begins to generate finite curvatures on an initially planar propagating surface with vanishing κ_i^* , and this term is dominant in Eq. (16). Thus the last term for $S_{d,\alpha\beta}$ can be neglected for $\text{Ma Ka} \ll 1$. On the other hand, neglecting the term $S_{d,\alpha\beta}$ may result in unacceptably large errors at large times. Therefore, the following results for nonconstant S_d are restricted to $\text{Ma Ka} \sim O(0.1)$ and $t/\tau_\eta \leq 2$.

In Fig. 10(a), the surviving ratio remains unity (without cusp formation) for negative Ma , and the surviving ratio for positive Ma is smaller than that for the case with constant S_d . This observation can be explained by the analysis from Eq. (15). In the cusp formation with $|\kappa_2^*| \gg |\kappa_1^*|$, the last term in Eq. (8) with a large negative κ_2^* dominates, so Eq. (15) can be approximated as

$$S_d^* - S_L^* \approx \text{Ma}(\text{Ka } S_L^*|\kappa_2^*|). \quad (17)$$

Thus for $\text{Ma} > 0$, statistically $S_d^* > S_L^*$ accelerates cusp formation. The acceleration of S_d of flame particles before extinction is also observed in DNS of turbulent premixed combustion [19]. For $\text{Ma} < 0$, $S_d^* < S_L^*$ inhibits cusp formation. Since more surface elements with negative κ_2^* for $\text{Ma} < 0$ can survive than those for $\text{Ma} > 0$, $|\langle \kappa_2^* \rangle|$ is larger for $\text{Ma} < 0$ than those for $\text{Ma} \geq 0$ in Fig. 10(c). The region on a global propagating surface with the large negative curvature corresponds to the pocket structure that causes the flame front to be unstable in fuel-lean turbulent premixed combustion [9,29].

On the other hand, for the surface elements with $|\kappa_1^*| > |\kappa_2^*|$ or $\kappa_1^* + \kappa_2^* > 0$, Eq. (15) implies that statistically $S_d^* > S_L^*$ for $\text{Ma} < 0$ and $S_d^* < S_L^*$ for $\text{Ma} > 0$. These elements with $|\kappa_1^*| > |\kappa_2^*|$ make the major contribution to $\langle \kappa_1^* \rangle$. In Fig. 10(b), $\langle \kappa_1^* \rangle$ is decreased with decreasing Ma from $\text{Ma} > 0$ to $\text{Ma} < 0$, which is also consistent with the result in Fig. 8(b).

V. SURFACE AREA RATIO

A. Evolution equation of the surface area

The surface area ratio A_T/A_0 is defined as the ratio of the flame surface area A_T in turbulence divided by its projection in the propagating direction A_0 , which is generally equal to the ratio of the turbulent burning speed to the laminar flame speed [5]. In the present study, A_T/A_0 is modeled as the surface area ratio of the global propagating surface in the statistical stationary turbulent state to the initial planar surface.

To derive the governing equation for A_T/A_0 , we first divide the initial planar surface into N_e surface elements. In the evolution of propagating surfaces, N_d surface elements disappear because they evolve into cusps at a certain time step and their surface area shrinks to zero [2]. Thus the total surface area of the global propagating surface consisting of N_s surviving surface elements is approximated as

$$A(t^*) \equiv \sum_{N_s(t^*)} \delta A(t^*), \quad (18)$$

and the initial surface area of the global surface is approximated as

$$A_0 = \sum_{N_e} \delta A_0. \quad (19)$$

The evolution equation of $A(t^*)$ is obtained by summing up the local quantities on $N_s(t^*)$ surviving surface elements in Eq. (11) as

$$\frac{d}{dt^*} A(t^*) = \sum_{N_s(t^*)} K_t^*(t^*) \delta A(t^*) + 2 \sum_{N_s(t^*)} S_d^*(t^*) \kappa^*(t^*) \delta A(t^*). \quad (20)$$

Dividing both sides of Eq. (20) by $A(t^*)$ yields

$$\frac{d}{dt^*} \ln A(t^*) = \langle K_t^*(t^*) \rangle_A + 2 \langle S_d^*(t^*) \kappa^*(t^*) \rangle_A, \quad (21)$$

where

$$\langle f(t^*) \rangle_A \equiv \frac{\sum_{N_s(t^*)} f(t^*) \delta A(t^*)}{A(t^*)} \quad (22)$$

denotes the area-weighted average of a function $f(t^*)$. It is noted that Eq. (22) can result in unacceptably large statistical errors at large times in the numerical implementation owing to sporadic occurrences of extremely large surface areas [43], so we only report the area-weighted averaged quantities at small times in the present study.

Integrating Eq. (21) on the trajectory of propagating surface elements from the initial tracking time to a given time t^* yields the surface area of the global propagating surface,

$$A(t^*) = A_0 \xi_K(t^*) \xi_p(t^*). \quad (23)$$

The increase of surface area is contributed from the tangential strain-rate term

$$\xi_K(t^*) \equiv \exp \left(\int_0^{t^*} \langle K_t^*(s^*) \rangle_A ds^* \right) \quad (24)$$

and the propagation-curvature term

$$\xi_p(t^*) \equiv \exp \left(2 \int_0^{t^*} \langle S_d^*(s^*) \kappa^*(s^*) \rangle_A ds^* \right). \quad (25)$$

B. Modeling of the area ratio

We remark that the surface area A_T of the premixed flame surface in turbulence can be considered as a stationary random variable with competing flame stretching and shortening mechanisms [44]. However, the propagating surface in the present study has $A(t^*) \rightarrow \infty$ as $t^* \rightarrow \infty$, because it has no flame shortening mechanism, which may occur when adjacent flamelets consume the intervening reactant, thereby annihilating both surface elements. Thus we model the turbulent flame surface area

$$A_T = A(T_s^*) \quad (26)$$

as the surface area of the global propagating surface at $t^* = T_s^* \equiv T_s / \tau_\eta$ when the curvature statistics just reach the statistically stationary state.

Finally, the surface area ratio is obtained as

$$\frac{A_T}{A_0} = \xi_K(T_s^*) \xi_p(T_s^*). \quad (27)$$

This model involves the Lagrangian history of the area-weighted averaged tangential strain rate and mean curvature in the wrinkling of a global propagating surface in turbulence.

In Fig. 11, the contributions from $\xi_K(t^*)$ and $\xi_p(t^*)$ to A/A_0 in Eq. (27) are calculated using numerical integration. We find that the contributions from tangential stretching and propagation curvature are positive and comparable. Nevertheless, most previous studies argue that the contribution of the propagation and local curvature to the flame area is only through the negative averaged mean curvature from Eq. (9), so they conclude that the propagation and local curvature tend to decrease

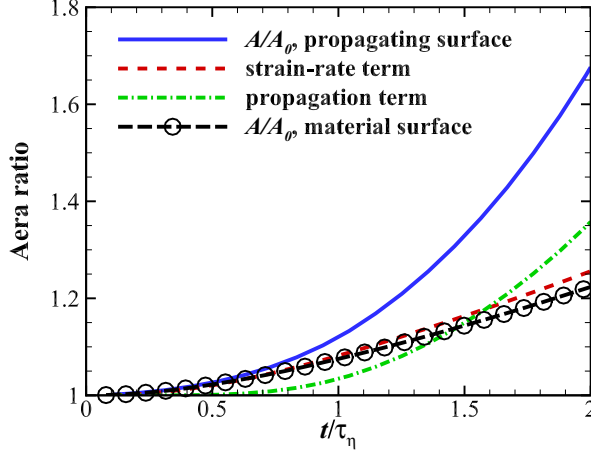


FIG. 11. Temporal evolution of the area ratios and two contributing terms in Eq. (27) with $S_d/u' = 1.0$, and the corresponding area ratio of material surface elements (with $S_d = 0$) in isotropic turbulence with $Re_\lambda = 110$.

A_T/A_0 on average [24,25,45]. This paradox is explained by different behaviors of $\langle \kappa \rangle$ and $\langle \kappa \rangle_A$ in Fig. 12. Although the averaged mean curvature is negative in Eq. (9), the area-weighted average is still positive in ξ_p in Eq. (27). The difference of $\langle \kappa \rangle$ and $\langle \kappa \rangle_A$ is related to the cellular geometry of the global propagating surface, and the nonlocal statistics and geometry [31,32] appear to be important in the modeling of turbulent premixed combustion. Furthermore, the contribution from $\xi_K(t^*)$ of propagating surface elements is very close to A/A_0 of evolving material surface elements without self-propagation. This implies that the propagation-curvature term directly contributes to the area increase of propagating surfaces, and it has a very minor effect on the stretching process by the tangential strain rate.

C. Cellular geometry

The cellular geometry is a signature geometric feature of flame fronts in premixed combustion owing to flame instabilities, particularly for lean fuels with $Ma < 0$ or the Lewis number less than

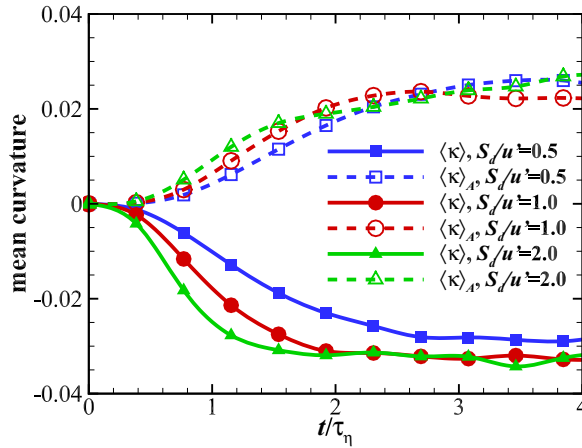


FIG. 12. Temporal evolution of unweighted and area-weighted averaged mean curvatures in isotropic turbulence with $Re_\lambda = 110$ and different S_d/u' .

unity. Similar to the flame fronts, the global propagating surfaces also show the cellular geometry in Fig. 3. The cellular geometry as sketched in Fig. 5 suggests that the total surface area of the surface elements with positive mean curvatures is much larger than that of the elements with negative mean curvatures. Furthermore, Eq. (9) implies that the surface element with positive κ is stretched, whereas the surface element with negative κ is compressed and even evolves into a cusp. Therefore, the difference of positive $\langle \kappa \rangle_A$ and negative $\langle \kappa \rangle$ in Fig. 12 characterizes the cellular geometry of a global propagating surface consisting of the elements with large δA and small positive κ and the elements with small δA and large negative κ .

As shown in Fig. 12, the differences of $\langle \kappa \rangle_A$ and $\langle \kappa \rangle$ with different S_d are increased in the temporal evolution of the global propagating surface, which agrees with the visualization of the emerging cellular structures in Fig. 3. The formation of the cellular structures appears to be faster for larger S_d than smaller S_d .

VI. CONCLUSIONS

The principal curvature statistics and surface area ratio of a global propagating surface in stationary homogenous isotropic turbulence at Taylor-scale Reynolds numbers from $Re_\lambda = 76$ to 185 are investigated using DNS and a revised algorithm for tracking propagating surface elements. A wide range of constant displacement speeds from $S_d/u' = 0.1$ to 5.0 and nonconstant displacement speeds with different Markstein numbers are considered.

The evolution of the global propagating surface consisting of 128^2 surface elements with a constant S_d shows that, from an initial plane, the surface is gradually wrinkled and corrugated to form the cellular geometry with the cusps generated near the pocket region in 2–3 Kolmogorov times. The statistics of principal curvatures are calculated over an ensemble of surviving surface elements without cusps. The joint PDF of the principal curvatures is similar to that of flame fronts from DNS of premixed combustion, which implies that the statistical result obtained from propagating surfaces can be useful in the modeling of premixed turbulent flames.

The statistical results are summarized as follows.

(1) The statistical profiles of the surviving ratio and principal curvatures $\langle \kappa_i^* \rangle$ scaled by the Kolmogorov length scale versus the displacement speed S_d^* scaled by the Kolmogorov velocity scale collapse for different Reynolds numbers.

(2) For different constant displacement speeds, $|\langle \kappa_1^* \rangle|$ decreases exponentially with increasing S_d^* , and $|\langle \kappa_2^* \rangle|$ decreases more mildly than $|\langle \kappa_1^* \rangle|$ with S_d^* .

(3) The surface-stretch effect on the nonconstant displacement speed can be modeled for very small Karlovitz numbers and tracking times, and this effect inhibits the surface element to evolve into a cusp at negative Markstein numbers.

(4) A model for estimating surface area ratio is developed. It depends on the Lagrangian history of the area-weighted averaged tangential strain rate and mean curvature in the wrinkling process of a global propagating surface in turbulence.

(5) The difference of the averaged and the area-weighted averaged mean curvatures characterizes the cellular geometry of the global propagating surface. The contribution from the area-weighted averaged mean curvature to the increase of the area ratio is positive.

The above conclusions can be valid for the evolution of propagating surfaces in isotropic turbulence at higher Reynolds numbers, and can be helpful for understanding the Lagrangian evolution of flamelets, nonlocal geometry of the flame front, and modeling of the flame surface density in premixed turbulent combustion in the flamelet regime. Further extension of propagating surfaces for studying the premixed combustion regimes of thin reaction and broken reaction zones should consider how to treat the topological changes in the evolution of surface elements. In addition, the Lagrangian-based modeling of turbulent burning velocity is expected to be developed from the surface area ratio and validated by combustion DNS and experimental data in future work.

ACKNOWLEDGMENTS

Y.Y. thanks Z. Chen for helpful comments. This work has been supported in part by the National Natural Science Foundation of China (Grants No. 91541204 and No. 11521091) and the Thousand Young Talents Program of China.

APPENDIX: CALCULATION OF THE CURVATURE TENSOR

In the numerical implementation for tracking propagating surface elements, we find that the curvature tensor $h_{\alpha\beta}$ can be slightly asymmetric, using the existing numerical method [2], owing to the accumulation of numerical errors. This results in imaginary principal curvatures calculated from $h_{\alpha\beta}$, so the time marching method for Eq. (5) is revised.

First, Eq. (5) for the curvature tensor can be reexpressed as

$$\frac{d\mathbf{h}}{dt} = \mathbf{G} + S_d \mathbf{h} \cdot \mathbf{h}, \quad (\text{A1})$$

where \mathbf{h} is the curvature tensor and

$$G_{\alpha\beta} = s_{33}h_{\alpha\beta} - (s_{\gamma\beta}h_{\alpha\gamma} + s_{\gamma\alpha}h_{\beta\gamma}) + U_{3,\alpha\beta} \quad (\text{A2})$$

is a second-order symmetric tensor, and the term $S_{d,\alpha\beta}$ in Eq. (5) is ignored.

In the implicit second-order Runge-Kutta method [2], the predictor tensor is

$$\mathbf{h}_1 = \mathbf{h} + (\mathbf{G}(\mathbf{h},t) + S_d \mathbf{h} \cdot \mathbf{h}_1)\Delta t, \quad (\text{A3})$$

which can be reexpressed as

$$\mathbf{h}_1 = (\mathbf{I} - S_d \mathbf{h} \Delta t)^{-1} \cdot (\mathbf{G}(\mathbf{h},t)\Delta t + \mathbf{h}). \quad (\text{A4})$$

Since \mathbf{h} is symmetric, the transpose of \mathbf{h}_1

$$\mathbf{h}_1^T = (\mathbf{h} + \mathbf{G}(\mathbf{h},t)\Delta t) \cdot (\mathbf{I} - S_d \mathbf{h} \Delta t)^{-1} \quad (\text{A5})$$

should be equivalent to \mathbf{h}_1 in principle, but \mathbf{h}_1 can be slightly asymmetric in the numerical implementation, so we use $\frac{1}{2}(\mathbf{h}_1 + \mathbf{h}_1^T)$ as an improved symmetric predictor tensor in the next corrector step.

The corrector tensor is calculated as

$$\mathbf{h}_2 = (\mathbf{I} - S_d \mathbf{h} \Delta t)^{-1} \cdot \left\{ \mathbf{h} + \frac{1}{2}[\mathbf{G}(\mathbf{h},t) + \mathbf{G}(\frac{1}{2}(\mathbf{h}_1 + \mathbf{h}_1^T),t + \Delta t)]\Delta t + \mathbf{H} \right\}, \quad (\text{A6})$$

where $\mathbf{H} \equiv \frac{1}{2}S_d(\mathbf{h}_1 \cdot \mathbf{h} - \mathbf{h} \cdot \mathbf{h}_1)\Delta t$ ensures that the scheme is second-order accurate. The symmetry of \mathbf{h}_2 and \mathbf{G} is improved based on $\frac{1}{2}(\mathbf{h}_1 + \mathbf{h}_1^T)$ instead of \mathbf{h}_1 used in [2]. Finally, we set

$$\mathbf{h}(t + \Delta t) = \frac{1}{2}(\mathbf{h}_2 + \mathbf{h}_2^T) \quad (\text{A7})$$

to maintain the symmetry of \mathbf{h} in the numerical implementation.

In addition, a criterion is proposed to monitor the cusp formation. If the second-order tensor $\mathbf{I} - S_d \mathbf{h} \Delta t$ defined in Eq. (A4) of a surface element is not positive definite at a time step t , $\mathbf{h}(t + \Delta t)$ goes to infinity in the implicit Runge-Kutta method. Thus we consider that the surface element evolves into a cusp at the next time step.

- [1] S. B. Pope, The evolution of surfaces in turbulence, *Int. J. Eng. Sci.* **26**, 445 (1988).
- [2] S. S. Girimaji and S. B. Pope, Propagating surfaces in isotropic turbulence, *J. Fluid Mech.* **234**, 247 (1992).
- [3] R. Yu, X. S. Bai, and A. N. Lipatnikov, A direct numerical simulation study of interface propagation in homogeneous turbulence, *J. Fluid Mech.* **772**, 127 (2015).
- [4] N. Peters, *Turbulent Combustion* (Cambridge University Press, Cambridge, 2000).
- [5] T. Poinso and D. Veynant, *Theoretical and Numerical Combustion*, 2nd ed. (Edwards, 2005).
- [6] H. Wenzel and N. Peters, Scaling of production, kinematic restoration, and dissipation of the mean flame surface area, *Combust. Sci. Technol.* **177**, 1095 (2005).
- [7] T. C. Treurniet, F. T. M. Nieuwstadt, and B. J. Boersma, Direct numerical simulation of homogeneous turbulence in combination with premixed combustion at low Mach number modelled by the G-equation, *J. Fluid Mech.* **565**, 25 (2006).
- [8] J. F. Driscoll, Turbulent premixed combustion: Flamelet structure and its effect on turbulent burning velocities, *Prog. Energy Combust. Sci.* **34**, 91 (2008).
- [9] J. H. Chen, T. Echekki, and W. Kollmann, The mechanism of two-dimensional pocket formation in lean premixed methane-air flames with implications to turbulent combustion, *Combust. Flame* **116**, 15 (1999).
- [10] M. Z. Haq, C. G. W. Sheppard, and R. Woolley, Wrinkling and curvature of laminar and turbulent premixed flames, *Combust. Flame* **131**, 1 (2002).
- [11] R. Balachandran, B. Ayoola, C. Kaminski, A. Dowling, and E. Mastorakos, Experimental investigation of the nonlinear response of turbulent premixed flames to imposed inlet velocity oscillations, *Combust. Flame* **143**, 37 (2005).
- [12] S. Gashi, J. Hult, N. Chakraborty, S. Cant, and C. F. Kaminski, Curvature and wrinkling of premixed flame kernels-comparisons of OH PLIF and DNS data, *Proc. Combust. Inst.* **30**, 809 (2005).
- [13] G. H. Markstein, Experimental and theoretical studies of flame fronts stability, *J. Aeronaut. Sci.* **18**, 199 (1951).
- [14] P. Pelcé and P. Clavin, Influence of hydrodynamics and diffusion upon the stability limits of laminar premixed flames, *J. Fluid Mech.* **124**, 219 (1982).
- [15] K. N. C. Bary and R. S. Cant, Some applications of Kolmogorov's turbulence research in the field of combustion, *Proc. R. Soc. London A* **434**, 217 (1991).
- [16] D. Bradley, P. H. Gaskell, A. Sedaghat, and X. J. Gu, Generation of PDFs for flame curvature and for flame stretch rate in premixed turbulent combustion, *Combust. Flame* **135**, 503 (2003).
- [17] L. Wang, E. R. Hawkes, and J. H. Chen, Flame edge statistics in turbulent combustion, *Proc. Combust. Inst.* **33**, 1439 (2011).
- [18] Y. Shim, S. Tanaka, M. Tanahashi, and T. Miyauchi, Local structure and fractal characteristics of H₂-air turbulent premixed flame, *Proc. Combust. Inst.* **33**, 1455 (2011).
- [19] H. A. Uranakara, S. Chaudhuri, H. L. Dave, P. G. Arias, and H. G. Im, A flame particle tracking analysis of turbulence-chemistry interaction in hydrogen-air premixed flames, *Combust. Flame* **163**, 220 (2016).
- [20] N. Peters, The turbulent burning velocity for large-scale and small-scale turbulence, *J. Fluid Mech.* **384**, 107 (1999).
- [21] V. L. Zimont, Gas premixed combustion at high turbulence. Turbulent flame closure combustion model, *Exp. Thermal Fluid Sci.* **21**, 179 (2000).
- [22] D. A. Knaus, S. S. Sattler, and F. C. Gouldin, Three-dimensional temperature gradients in premixed turbulent flamelets via crossed-plane Rayleigh imaging, *Combust. Flame* **141**, 253 (2005).
- [23] Y.-C. Chen, Measurements of three-dimensional mean flame surface area ratio in turbulent premixed Bunsen flames, *Proc. Combust. Inst.* **32**, 1771 (2009).
- [24] A. Trouvé and T. Poinso, The evolution equation for the flame surface density in turbulent premixed combustion, *J. Fluid Mech.* **278**, 1 (1994).
- [25] N. Chakraborty and S. Cant, Effects of strain rate and curvature on surface density function transport in turbulent premixed flames in the thin reaction zones regime, *Phys. Fluids* **17**, 065108 (2005).
- [26] A. N. Lipatnikov and J. Chomiak, Turbulent flame speed and thickness: phenomenology, evaluation, and application in multi-dimensional simulations, *Prog. Energy Combust. Sci.* **28**, 1 (2002).
- [27] S. B. Pope, P. K. Yeung, and S. S. Girimaji, The curvature of material surfaces in isotropic turbulence, *Phys. Fluids A* **1**, 2010 (1989).

- [28] S. S. Girimaji and S. B. Pope, Material-element deformation in isotropic turbulence, *J. Fluid Mech.* **220**, 427 (1990).
- [29] J. B. Bell, M. S. Day, and M. J. Lijewski, Simulation of nitrogen emissions in a premixed hydrogen flame stabilized on a low swirl burner, *Proc. Combust. Inst.* **34**, 1173 (2013).
- [30] S. B. Pope and W. K. Cheng, The stochastic flamelet model of turbulent premixed combustion, *Proc. Combust. Inst.* **22**, 781 (1989).
- [31] Y. Yang, D. I. Pullin, and I. Bermejo-Moreno, Multi-scale geometric analysis of Lagrangian structures in isotropic turbulence, *J. Fluid Mech.* **654**, 233 (2010).
- [32] Y. Yang, Identification, characterization, and evolution of non-local quasi-Lagrangian structures in turbulence, *Acta. Mech. Sin.* **32**, 351 (2016).
- [33] F. Toschi and E. Bodenschatz, Lagrangian properties of particles in turbulence, *Annu. Rev. Fluid Mech.* **41**, 375 (2009).
- [34] S. Chaudhuri, Life of flame particles embedded in premixed flames interacting with isotropic turbulence, *Proc. Combust. Inst.* **35**, 1305 (2015).
- [35] A. M. Steinberg, B. Coriton, and J. H. Frank, Influence of combustion on principal strain-rate transport in turbulent premixed flames, *Proc. Combust. Inst.* **35**, 1287 (2015).
- [36] Y. Yang, G.-W. He, and L.-P. Wang, Effects of subgrid-scale modeling on Lagrangian statistics in large-eddy simulation, *J. Turbul.* **9**, 8 (2008).
- [37] T. Ishihara, Y. Kaneda, M. Yokokawa, K. Itakura, and A. Uno, Small-scale statistics in high-resolution direct numerical simulation of turbulence: Reynolds number dependence of one-point velocity gradient statistics, *J. Fluid Mech.* **592**, 335 (2007).
- [38] D. A. Donzis, P. K. Yeung, and K. R. Sreenivasan, Dissipation and enstrophy in isotropic turbulence: Resolution effects and scaling in direct numerical simulations, *Phys. Fluids* **20**, 045108 (2008).
- [39] P. K. Yeung and S. B. Pope, An algorithm for tracking fluid particles in numerical simulations of homogeneous turbulence, *J. Comput. Phys.* **79**, 373 (1988).
- [40] Tecplot, Inc., <http://www.tecplot.com>.
- [41] S. S. Girimaji, Asymptotic behavior of curvature of surface elements in isotropic turbulence, *Phys. Fluids A* **3**, 1772 (1991).
- [42] M. Matalon, Flame dynamics, *Proc. Combust. Inst.* **32**, 57 (2009).
- [43] P. K. Yeung, S. S. Girimaji, and S. B. Pope, Straining and scalar dissipation on material surfaces in turbulence: Implications for flamelets, *Combust. Flame* **79**, 340 (1990).
- [44] F. E. Marble and J. E. Broadwell, The coherent flame model for turbulent chemical reactions, TRW report, 1977 (unpublished).
- [45] E. R. Hawkes and J. H. Chen, Evaluation of models for flame stretch due to curvature in the thin reaction zones regime, *Proc. Combust. Inst.* **30**, 647 (2005).